Materials Science & Engineering A 828 (2021) 142010

Contents lists available at ScienceDirect

Materials Science & Engineering A

journal homepage: www.elsevier.com/locate/msea

Strain distribution and lattice rotations during in-situ tension of aluminum with a transmodal grain structure

W.Q. Gao [a], C.L. Zhang [a], M.X. Yang [b], S.Q. Zhang [a,c,1], D. Juul Jensen [d], A. Godfrey [a,*]

[a] Key Laboratory of Advanced Materials (MOE), School of Materials Science and Engineering, Tsinghua University, Beijing, 100084, China
[b] State Key Laboratory of Nonlinear Mechanics, Institute of Mechanics, Chinese Academy of Sciences, Beijing, 100190, China
[c] State Key Laboratory of Refractories and Metallurgy, Wuhan University of Science and Technology, Wuhan, Hubei, 430081, China
[d] Department of Mechanical Engineering, Technical University of Denmark, DK-2800 Kgs, Lyngby, Denmark

ARTICLE INFO

Keywords:
Heterogenous grain structure
Strain distribution
High-resolution digital image correlation (HR-DIC)
Near-micrometer grain size
Electron backscatter diffraction (EBSD)

ABSTRACT

Samples of aluminum were prepared using spark plasma sintering from a mixture of coarse (average particle size of 6 μm) and fine (average particle size of 1 μm) powders to achieve a heterogeneous transmodal grain size distribution covering a range of grain sizes from ≈1 to 10 μm. By careful choice of surface markers both electron back-scatter diffraction (EBSD) data, to track crystal rotations, and digital image correlation (DIC) data, to track local plastic deformation, were collected from the same region during in-situ tensile deformation up to a strain of $\varepsilon_t = 0.126$. A heterogeneous pattern of crystal rotation is observed for all grain sizes, although in some smaller grains (defined as those <4 μm diameter) no clear grain sub-division was identified. Plastic strain was more concentrated in the larger grains, but the average rotation rate of the smaller grains was found to be higher than that of larger grains, showing also a much wider spread in rotation rate. Based on the change in average orientation, a clear orientation dependence in the tensile axis rotation direction was observed for many larger grains, in agreement with previously reported data for aluminum with average grain size of 75 μm, whereas the smaller grains showed a more complex rotation behavior, with more of these grains showing unexpected tensile axis rotations. The combination of both EBSD and DIC during in-situ experiments provides a rich data set for analysis of plastic deformation in samples with a heterogeneous microstructure.

1. Introduction

Metals and alloys with sub-micron and near-micron grain size exhibit some distinctive mechanical properties, including softening by deformation, hardening by annealing [1], a significant yield drop, and limited uniform elongation due to the onset of plastic instability [2–5]. At the same time, the mechanical properties are typically sensitive to grain size, and undergo a significant transition as the grain size increases from sub-micron values to several microns [4,5]. It is of interest therefore to investigate the deformation behavior and mechanisms in the near-micrometer scale where such a transition exists. Additionally materials with heterogeneous microstructures have attracted extensive attention in recent years due to the potential of realizing a good strength-ductility synergy in such microstructures [6–8]. A wide variety of tailored microstructures for heterostructured materials have been proposed, including gradient structures [9,10], laminate structures [11], harmonic structures [12], hierarchical structures [13], bi-modal structures [14] and dual phase structures [15], where in many cases a variation in grain size forms a key part of the microstructural heterogeneity. For bi-modal grain-size microstructures, it has been suggested that a good balance of high strength and good ductility can be achieved in cases where the fine grains provide high strength while coarser grains allow large elongation and improve the ductility effectively during tensile deformation [16–18]. However, the deformation mechanisms in such materials have not yet been clarified and little research has been carried out on the relationship between local strain distribution and microstructure evolution in such microstructures. Moreover, the applicability of these ideas to microstructures with only relatively small differences in grain size, but where these differences also straddle a transition in mechanical properties, distinguished here by the name transmodal, remains an open question.

Many different processes to obtain bi-modal grain structures in

* Corresponding author.
E-mail address: awgodfrey@mail.tsinghua.edu.cn (A. Godfrey).
[1] present address.

https://doi.org/10.1016/j.msea.2021.142010
Received 24 March 2021; Received in revised form 31 August 2021; Accepted 31 August 2021
Available online 1 September 2021

metals and alloys have been proposed, divided loosely into two: those relying on severe plastic deformation followed by appropriate heat treatments [19–21] or those based on powder metallurgy [22–24] by controlled mixing of powders with different powder particle sizes. For the latter it has been demonstrated that the spark plasma sintering technique (SPS) can be used to obtain almost fully dense samples with near-micrometer grain size in a fully recrystallized condition with a low dislocation density and random texture [25], as required for a controlled study of deformation mechanisms [2,26]. In particular the grain size of aluminum samples sintered by SPS can be controlled by the initial powder size [2] due the native oxide film present on the surface of each powder particle, providing thereby a method to prepare samples with a designed microstructure by tailoring the size and distribution of powder particles.

Regarding studies of the relationship between plastic deformation mechanisms and local microstructural characteristics, two important techniques are digital image correlation (DIC) [27,28] and electron back-scatter diffraction (EBSD) [29]. These techniques provide complimentary data in the context of studies of plastic deformation, where DIC can be used to obtain the local distribution of surface displacements (and hence information related to plastic strain), and EBSD provides spatially-resolved information over large areas on the local crystal lattice reorientations that accompany plastic deformation [29,30]. A requirement for collection of DIC data is the presence of a high contrast pattern of appropriate spatial resolution on the sample surface to provide markers for tracking of surface displacements [31]. For this purpose a variety of patterning techniques have been investigated, including focused ion beam (FIB) patterning [32], electron beam lithography [33], template patterning [34], thin film ablation [35,36] and nanoparticle deposition techniques [37,38]. A further challenge here is that while DIC and EBSD provide complimentary data, in general the surface patterning required for DIC measurements prevents the collection of high quality EBSD data, limiting the scope for in-situ deformation experiments where both types of data are collected over a number of strain steps.

Recently Zhang et al. [39] demonstrated a method based on a two-step electropolishing technique, utilizing controlled pitting, that allows such a limitation to be overcome. The spatial resolution of the two-step electropolishing technique is, however insufficient for the study of deformation of samples with a near-micrometer grain size. Instead, in this work we demonstrate that combined EBSD and sub-micrometer resolution DIC measurements over a number of strain steps can be achieved by use of a dispersion of colloidal silica particles as surface markers [40]. The results are used to investigate the influence of grain size on the local crystal rotations during in-situ tension of an aluminium sample with a transmodal grain-size distribution, with grain sizes in the near-micrometer regime.

2. Material and methods

Samples were prepared from a mixture of 6 μm and 1 μm (average particle size) aluminum powders with volume fractions of 63% and 37%, respectively. The Al powder purity was 99.9%, with native surface oxide thickness of 32 nm (6 μm powder) and 10 nm (1 μm powder) [2]. Powder mixing was carried out by stirring in alcohol for 30 min, followed by ultrasonic vibration for 30 min to break up particle aggregation, and then additional stirring for 60 min. The mixed powder was dried at 80 °C for 16 h in vacuum and then sintered using SPS according to the process in Ref. [2] to form disks of 20 mm diameter, resulting in samples with a density of >99.4%.

Tensile dog-bone samples, based on a scaled down version of the ASTM E8/E8M-09 geometry, were cut using electron-discharge machining (EDM) from the as-sintered disks with gauge length, width, and thickness of 8.0, 1.8 and 0.6 mm, respectively. All surfaces were ground flat to remove the influence of EDM damage. To investigate the evolution of both strain distribution and crystal lattice rotations using in-situ HR-DIC and EBSD techniques, the upper surface of a tensile sample was first electrochemically polished to a mirror finish. Colloidal silica (OPS) solution of a 1:9 dilution was given 2 h of ultrasonic vibration to break up particle aggregates, then dropped onto the sample surface to achieve a uniform distribution of SiO_2 particles as markers for DIC measurements. This dilution was found to be optimal for the present experiment, but in general the dilution should be determined considering both the particle concentration in the OPS stock solution and the desired DIC window size. Once dried the SiO_2 particles exhibit good mechanical stability and strong surface adherence, as verified by a series of tests where a patterned sample was subjected both to mechanical agitation and ultrasonic vibration in ethanol for 30 min (after which no detectable change in the particle distribution was observed). After visual inspection hardness indentations were made on the sample surface to identify a region of interest, as well as to facilitate alignment of the sample in the scanning electron microscope (SEM) and to allow a direct measurement of the strain applied during tensile loading. Further details regarding the sample preparation process are given elsewhere [40].

For the in-situ tension experiments the sample was mounted on a push-to-pull stage, coupled to a load cell for measurement of the instantaneous force. The EBSD and DIC measurements were carried out using a TESCAN MIRA 3 SEM equipped with a CMOS-based EBSD detector (Oxford Instruments). Secondary electron (SE) images were recorded for the DIC measurements using a 5 kV operating voltage over an area of $69.2 \times 69.2\ \mu m^2$, mapped using an image size of 4096×4096 pixels. Images for DIC analysis were collected before tensile testing and after deformation to strains of $\varepsilon_t = 0.006$, 0.040, 0.077 and 0.126, where these values are the average Lagrangian strain along the tensile loading axis for the entire region tracked during the experiment. The VIC 2D software package was used for the DIC calculations, in each case using a subset size of 59×59 pixels ($\approx 1.0 \times 1.0\ \mu m^2$) and a step-size (window offset) of 3 pixels.

For the EBSD data, maps covering the same region of interest were collected over an area of $60 \times 60\ \mu m^2$ at a step size of 0.15 μm using a 20 kV operating voltage. Due to the known effects of surface contamination, EBSD data were only acquired in the undeformed (initial) state, after strains of $\varepsilon_t = 0.040$, and after the final applied strain of $\varepsilon_t = 0.126$. Analysis of the EBSD data was carried out using commercially available post-processing software as well as codes developed in-house. Only minimal data cleaning was applied to the EBSD data (three operations of the noise-reduction algorithm on a setting of 5/8 neighbors in the Oxford Instruments Channel 5 software).

For grain tracking in the in-situ deformation experiment, a grain detection algorithm was first applied using a 2° misorientation angle definition to the undeformed data. The as-detected grains were then manually propagated to the two deformed conditions. Only grains that could be identified at every deformation step were included in the analysis. Edge-grains were handled as described in section 4.1. Of the 569 grains in the undeformed EBSD map, 493 were tracked until the largest applied strain (87% by grain number). All grain sizes are reported as equal circle diameter values, $d_{ECD} = 2\sqrt{(A/\pi)}$, where A is the area of each grain determined in the grain detection algorithm. All data acquisition (DIC and EBSD) for the in-situ experiment was carried out without removing the sample from the tensile stage. All EBSD and DIC maps relating to the in-situ experiment in this paper are shown with the tensile axis parallel to the horizontal page direction.

An additional set of tensile tests were carried out at room temperature using an Instron 5966 universal material testing instrument on the mixed powder SPS samples, as well as on SPS samples made using either only 6 μm powder or the 1 μm powder. These tests were carried out on samples of the same size as for the in-situ experiment, under displacement control at an initial strain rate of $2.1 \times 10^{-3}\ s^{-1}$ using a contact extensometer with gauge length of 5 mm.

3. Results

3.1. Mixed-powder sample microstructure

An example EBSD image of the as-sintered sample, covering an area of 100 × 100 μm^2 is shown in Fig. 1a. Good mixing of the 1 μm and 6 μm powders can be seen without the presence of extensive heterogenous agglomeration of either powder. The grain size (d_{ECD}) distribution is shown in Fig. 1b, where for better visualization the frequency is weighted by grain diameter (i.e. where the value of each bin is multiplied by the mean bin value, effectively plotting relative area fraction against grain size), revealing that the mixed powder sample exhibits an overlapping bimodal grain size distribution. Fig. 1b shows this same data in cumulative format (discussed further in section 3.5).

The distribution of SiO_2 particles used as DIC markers in this work can be seen in Fig. 2, showing an area near the center of the tracked region in this combined DIC and EBSD investigation. The figure illustrates that a good coverage of nano-scale markers is achieved, with SiO_2 particle size varying in the range from ≈20 nm to 120 nm. The higher magnification inset illustrates the 59 × 59 pixels window used for the DIC calculations, corresponding to a size of ≈1.0 × 1.0 μm^2.

Tensile strain-stress curves obtained using a standard laboratory testing frame for samples prepared wholly from 1 μm Al powder and 6 μm Al powder, as well as for a sample prepared from the mixed powder, are shown in Supplementary Material Fig. S1. Investigation using EBSD revealed average grain sizes for these samples of 1.2 μm (for the 1 μm powder sample) and 4.4 μm (for the 6 μm powder sample). The mixed powder sample has a flow curve exhibiting a good combination of both high strength and good ductility, falling in the transition regime between conventional yielding (6 μm powder sample) and negligible ductility (1 μm powder sample). A summary of the tensile properties of all three samples is given in Table 1.

3.2. Lattice rotations during in-situ tensile deformation

EBSD mapping of the undeformed sample resulted in a high indexed fraction of 95% (before the data cleaning as described in Section 2), with almost all of the non-indexed points located along grain boundaries. This high indexed fraction confirms that the fine-scale SiO_2 DIC markers do not adversely affect the EBSD data acquisition. In the EBSD map collected at the final strain of $\varepsilon_t = 0.126$ an increase in the fraction of non-indexed map pixels is seen as a result of surface roughening due to the plastic deformation and contamination from the repeated mapping, with most of these located, however, in the smallest grain size regions.

An initial qualitative assessment of the local lattice rotations developed during tensile loading was carried out by construction of the kernel average misorientation (KAM) at each pixel (calculated here using a square 3 × 3 kernel with an upper cut-off angle of 2°). After a tensile strain of $\varepsilon_t = 0.040$ locally higher KAM values are observed predominantly in the larger grains, whereas after $\varepsilon_t = 0.126$ locally higher KAM values are seen also in many small grains, with some evidence already at this strain for the presence of well-defined low angle dislocation boundaries inside some of the grains. These observations are illustrated further in Supplementary Material Fig. S2, which show EBSD maps using inverse pole-figure coloring and KAM value of the tracked area both before deformation and after local average tensile strains of $\varepsilon_t = 0.040$ and 0.126.

As a result of the in-situ tensile loading it is possible to analyze the lattice rotation at each individual pixel during loading, providing information that can be directly compared with predictions from a crystal

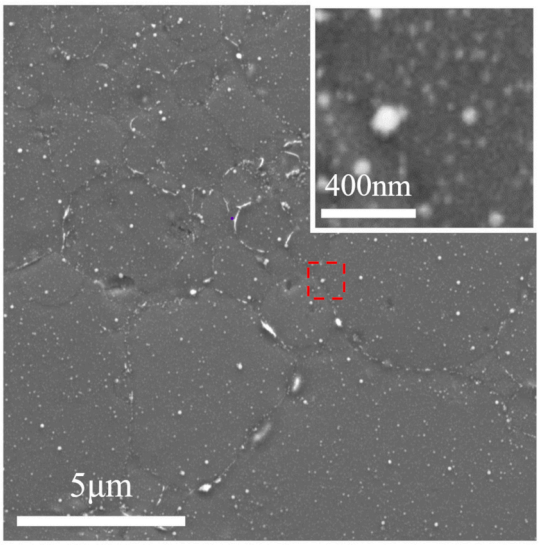

Fig. 2. SEM image illustrating the size and distribution of the SiO_2 DIC markers near the center of the tracked region in this combined DIC-EBSD study. The inset is a magnified view showing the 59 × 59 pixel window used for the DIC calculations.

Table 1
Summary of mechanical properties for both single powder and mixed powder samples: yield strength (YS), ultimate tensile strength (UTS) and uniform elongation (EL).

Powder size (grain size)	YS (MPa)	UTS (MPa)	EL (%)
1 μm (1.2 μm)	189	189	–
37% 1 μm/63% (6 μm)	95	123	16
6 μm (4.4 μm)	67	103	23

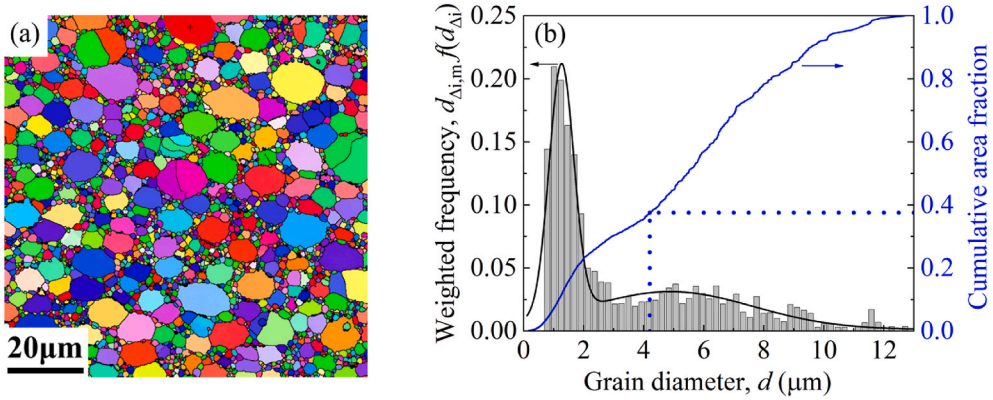

Fig. 1. EBSD measurements on the as-prepared SPS mixed powder material: (a) map showing an example region; (b) grain-size distribution shown as relative frequency multiplied by the bin mid-value (left-side axis), i.e., $d_{\Delta i,m}N(d_{\Delta i})/N(\text{total}) = d_{\Delta i,m}f(d_{\Delta i})$, where Δ_i represents the contents of the i-th bin with grain diameter, d, and in cumulative area fraction format (right-side axis), plotting $A(d < d_i)/A(\text{total})$ as a function of grain diameter (the blue dotted lines show that 0.375 (37.5%) of the map area corresponds to grains with diameter less than 4.2 μm). (For interpretation of the references to color in this figure legend, the reader is referred to the Web version of this article.)

plasticity analysis. This calculation is performed by determining misorientation of each pixel *i* (with measured crystal orientation of $\boldsymbol{g}_i$) to the orientation of the grain containing that pixel in the undeformed state ($\boldsymbol{g}_u$), as ${}^s\boldsymbol{R}_{u,i} = \boldsymbol{g}_u{}^{-1}\boldsymbol{g}_i$. Note that for the standard definition of the orientation matrix, $\boldsymbol{g}$, this gives the misorientation described in the sample frame (indicated here by the superscript, s). The results are shown in Fig. 3a-d, where ${}^s\boldsymbol{R}_{u,i}$ is decomposed into the angle component, $\theta_{u,i}$ and the axis component, ${}^s[uvw]_{u,i}$, for samples deformed to strains of $\varepsilon_t = 0.040$ and 0.126.

Both the angle and axis maps show a heterogeneous pattern of lattice rotation, on the intra- as well as the inter-grain level. After a strain of $\varepsilon_t = 0.040$ (Fig. 3a) the largest lattice rotation angles are associated mainly with larger grains, but some small grains also show comparable lattice rotations, and many large grains only show relatively small lattice rotations. Heterogeneity of lattice rotation angle within individual grains takes different forms: in some cases this extends in a region across entire grains, while in other cases regions of higher lattice rotation are connected to grain boundary or triple point regions. This agrees well with earlier observations [41,42]. At $\varepsilon_t = 0.126$ the extent of heterogeneity in lattice rotation angle (both intra- and inter-grain) is greater than at the lower strain, and in most grains the intra-grain rotations show a similar pattern to those already established at the lower strain.

Interpretation of the axis-component maps is less straightforward, with a suggestion of some macroscale variation (for example most of the grains in the upper-right quadrant show a similar lattice rotation direction). Some heterogeneity in the pattern of grain-scale subdivision (i.e., different parts of a grain rotating in different directions) is seen already at $\varepsilon_t = 0.040$, though this is much more pronounced at $\varepsilon_t = 0.126$, where a majority of the larger grains show some intra-grain variation in rotation axis. In contrast most of the smaller grains, including those with a large rotation angle component, show a similar rotation axis over the whole grain.

It is instructive also to construct maps of the misorientation between the grain average orientation and each map pixel ($\boldsymbol{R}_{av,i}$), noting that such maps can be constructed even for "snapshot" data sets where individual grains are not tracked during an in-situ experiment. In particular it has been shown [43] that even at low plastic strains, where local crystal misorientations are small and in many cases below the resolution that can be achieved using standard EBSD procedures, clear evidence of grain subdivision can be revealed from maps showing the rotation axis component of the pixel-to-grain average misorientation expressed in the sample coordinate frame, ${}^s[uvw]_{av,i}$. Examples of such maps are shown in Supplementary Material Fig. S3(a-c).

For the undeformed sample (Fig. S3a) many of the grains show a characteristic random color speckle noise. This arises from the fact that the grains are essentially recrystallized so that the misorientation angle between each pixel and grain average is very small, and thus the axis component exhibits a high variance and is poorly defined [44]. It can be noted, however, that in some grains regions of preferred color are visible. These originate from the presence of very low angle variations within the grains, where the orientation change is too delocalized to be picked up by either a boundary map or a KAM map (i.e., the change in orientation takes place over a few pixels).

The large difference in appearance in the ${}^s[uvw]_{av,i}$ map after tensile deformation to $\varepsilon_t = 0.040$ results from small systematic lattice rotations developed within each grain during straining. Although some care must be taken in interpreting such maps, in general within any grain each region of a single color represents parts of the grain that have rotated differently to parts with other colors, and therefore tracks a process of grain subdivision. Increasing the strain to $\varepsilon_t = 0.126$ results in some further enhancement of the contrast between different regions. It is interesting to observe, however, that the dominant pattern of

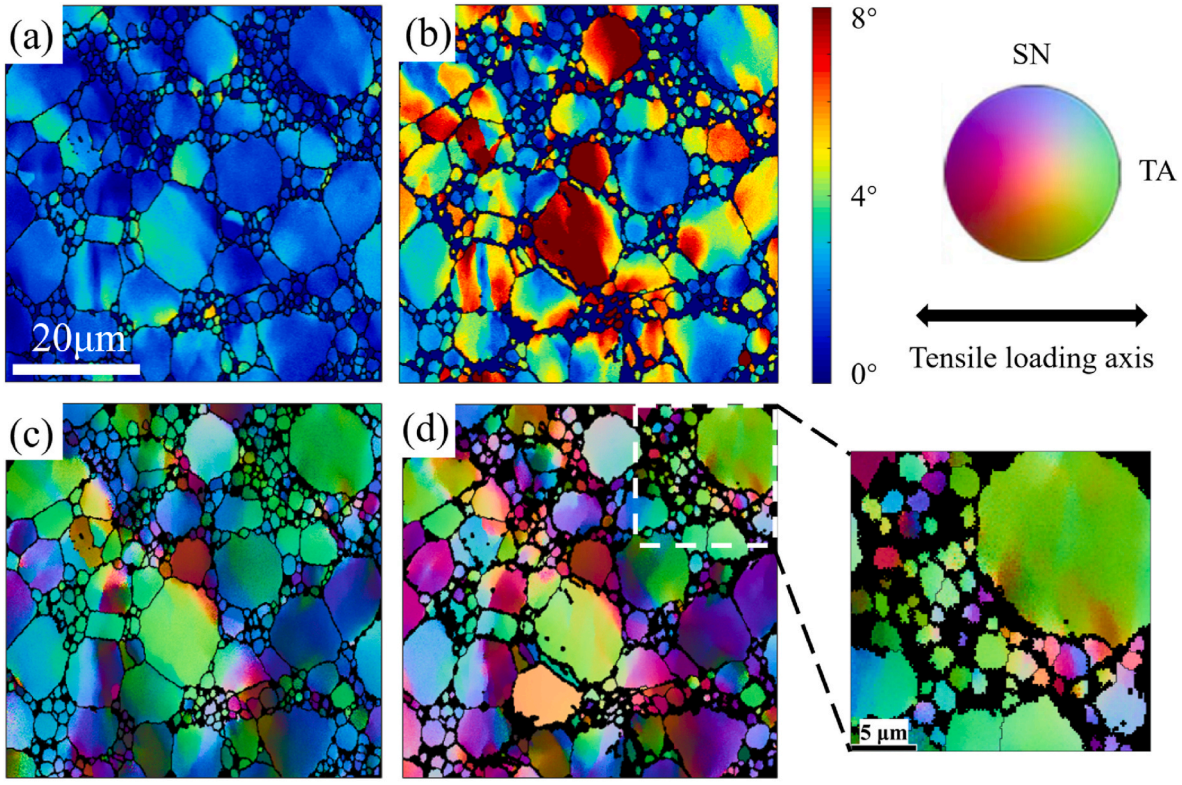

Fig. 3. Analysis of misorientation lattice rotation with respect to the initial (average) grain orientation: angle component $\varepsilon_t = 0.040$ (a) and $\varepsilon_t = 0.126$ (b); axis component (expressed in sample frame) at $\varepsilon_t = 0.040$ (c) and at $\varepsilon_t = 0.126$ (d); the inset to (d) shows a magnified view of the area indicated by a white dashed frame to show more clearly the rotation pattern in the smaller grains. The vertical color bar shows the misorientation angle for (a) and (b); the projected upper hemisphere shows the misorientation axis distribution for (c–d). TA = tensile axis (horizontal as indicated in the figure); SN = sample normal. (For interpretation of the references to color in this figure legend, the reader is referred to the Web version of this article.)

subdivision in many grains remains similar to that already established at the lower strain. A closer analysis reveals that whereas obvious subdivision is seen in most of the larger grains, this is not the case for many of the smaller grains (identified by a random-color speckle pattern).

3.3. Local strain distribution

Maps obtained from the DIC calculations showing the spatial distribution of the tensile (ε_{xx}) in-plane strain component after loading to $\varepsilon_t =$ 0.006, 0.040 and 0.126 are shown in Fig. 4a-c. To aid visual inspection of the data, black lines showing the grain boundaries are overlaid on the DIC maps. For strains of $\varepsilon_t = 0.040$ and 0.126 these are taken from the EBSD data; for $\varepsilon_t = 0.006$, where no EBSD map was taken, the undeformed EBSD map is used.

The spatial distribution of ε_{xx} is largely similar at each strain level, with a clear pattern of strain heterogeneity seen already developed after the first small strain increment ($\varepsilon_t = 0.006$), although this is much weaker than at the larger strains. With just a few exceptions the highest local strains at each strain step are seen in the larger grains. Similarly, regions associated with the lowest relative strain in each map are in general found to correspond to locations containing groups of small grains, though it can also be seen that some small grains also are associated with relatively large strains, and in some cases with an intra-grain strain localization. Fig. 4d shows an electron channeling contrast image of the tracked area after the final deformation step.

A number of slip traces can be observed in many of the larger grains, whereas no obvious slip traces are visible in the regions composed of smaller grains. In the large grain in the center of the map the alignment of these slip bands agrees well with the pattern of intra-grain strain heterogeneity from the DIC calculations. It is worth noting that the persistence of the macroscopic strain concentration during in-situ loading does not conflict with latent hardening, as deformation is instead transferred locally to nearby slip planes, rather than becoming uniformly distributed across many grains, helped by the ease of cross-slip in aluminum.

Inspection of the DIC maps in Fig. 4 reveals a complex variation also in the presence of location of strain gradients within both the coarse grains and in fine-grain regions, with no clear evidence for example of systematic strain gradients inside coarse grains adjacent to fine-grain regions. As such we have not been able to find any simple scalar measure of strain gradient associated with each grain that can be easily analyzed in an instructive manner. Instead, in this work we focus on the average grain strain as the main parameter for analysis of the DIC data. As shown in section 3.5, combined with the ability to collect both EBSD and DIC data during in-situ deformation, this allows, for the first time to the authors' knowledge, the evolution of the strain-normalized average grain rotation to be determined, providing also valuable data for the crystal plasticity modelling community.

3.4. Grain-average based analysis of strain and rotation

In order to examine the relationship between grain size and strain distribution the average ε_{xx} strain associated with each grain (referred to hereafter as ${}^{g}\varepsilon_{xx}$) was determined using an in-house Matlab code, taking as inputs both the DIC maps at each strain level and the grain structure identified from the EBSD data. The results for tensile strains of $\varepsilon_t = 0.040$ and 0.126 are summarized Fig. 5, where the average tensile strain for each grain is plotted as a function of the initial grain diameter (maps showing grain average strain values are shown in Supplementary Information Figs. S4a and b). At both strain levels cases a wide variation in ${}^{g}\varepsilon_{xx}$ for all grain sizes is observed, though many of the lowest grain-average strains are associated with regions containing small grains.

Data points in Fig. 5 with an attached horizontal line indicate edge grains, with the right-hand end-point of the horizontal line showing the estimated diameter in the investigated sample section as described in the following. Small edge-grains ($d_{ECD} < 5$ μm in the tracked area) were

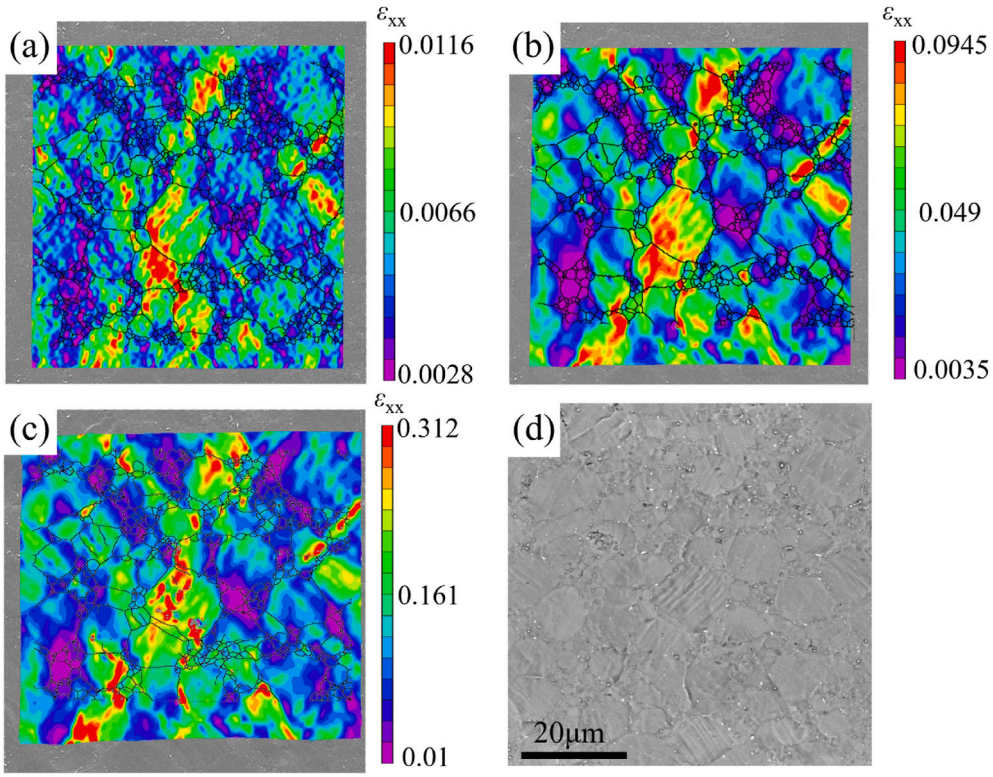

Fig. 4. DIC results showing the variation of local tensile (ε_{xx}) strain of after loading to average strains of (a) $\varepsilon_t = 0.006$, (b) $\varepsilon_t = 0.040$ and (c) $\varepsilon_t = 0.126$. Grain boundary positions (obtained from EBSD mapping) are overlaid in black in (a, b, c); (d) electron channeling contrast image of the examined area after a strain of $\varepsilon_t =$ 0.126. The tensile loading axis is parallel to the scale bar in (d).

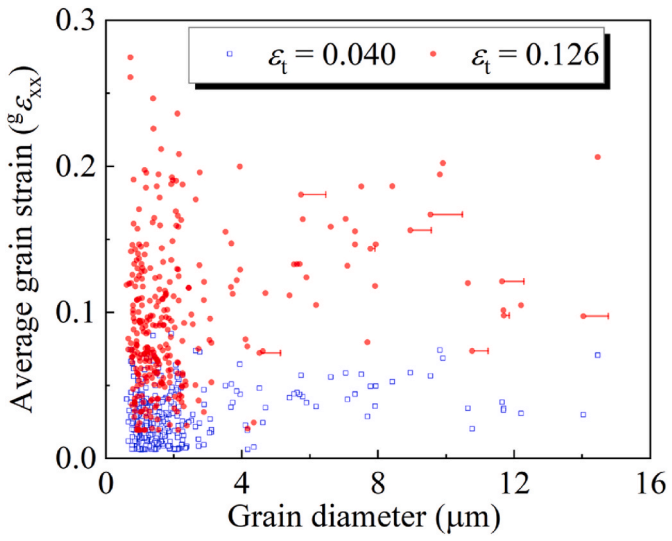

Fig. 5. Average strain for each grain as a function of initial grain diameter after deformation to $\varepsilon_t = 0.040$ and $\varepsilon_t = 0.126$. Points with horizontal lines attached represent grains at the map edge (only shown for $\varepsilon_t = 0.126$) and indicate the difference between diameter based on the mapped grain area (left-hand side marker) and the estimated full grain area in the tracked plane (right-hand side line end-point) Fig. 6 gives further details of the handling of map-edge grains.

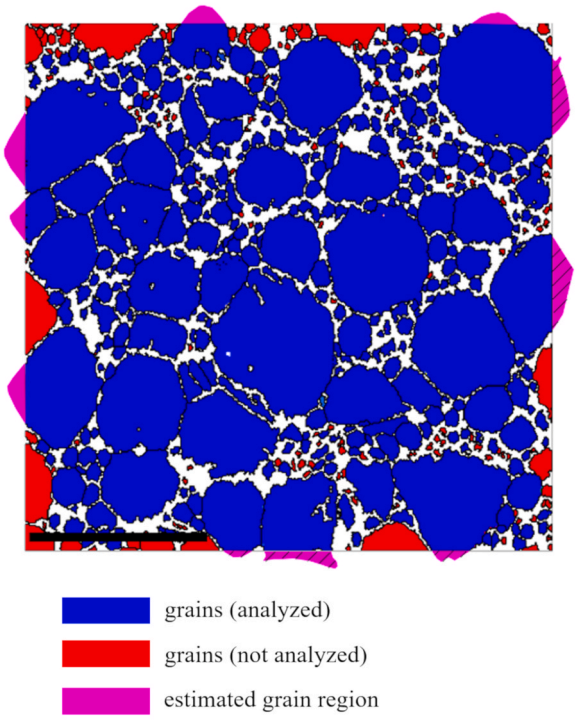

Fig. 6. Grains tracked and analyzed in the in-situ experiment are shown in blue; magenta colored areas show the estimated full grain area in this section of edge-grains included in the analysis (areas with hatching are based on direct observation of the grain shape from other EBSD maps; areas without hatching are best-guesses based on a typical grain shape). Red colored areas are for grains which are either estimated to be less than 50% characterized in all maps or less than 20 pixels in area, and thus ignored in the analysis. The black scale bar represents 20 μm. White areas indicate areas with no EBSD indexing in the final strain step. (For interpretation of the references to color in this figure legend, the reader is referred to the Web version of this article.)

ignored. For all other edge grains, the grain diameter in this section was taken, where visible, from the lower strain maps (as these covered a slightly larger area), and in other cases from an estimation of the expected grain shape. Grains were only included in the analysis if the observed area at any strain was estimated to cover more than 50% of the grain-section. Very small grains in the tracked area (defined as those with area of less than 20 pixels, i.e., $d_{ECD} < 0.75$ μm in the initial undeformed state) were also ignored. Fig. 6 illustrates the grains included in all subsequent quantitative analysis in this paper based on these definitions.

As can be seen from Fig. 5, the values of $^g\varepsilon_{xx}$ for the larger grains after an applied tensile strain of $\varepsilon_t = 0.126$ lie mostly in the range from 0.1 to 0.2, while the smaller grains are associated with a wider spread in $^g\varepsilon_{xx}$, with the largest average strains found for some of these grains. The majority of the smaller grains, however, have a $^g\varepsilon_{xx}$ strain value of less than the average over all grains ($\varepsilon_t = 0.126$). Comparison with the data at the lower tensile strain of $\varepsilon_t = 0.040$ shows that for some grains there is only a relatively small increase in the average grain strain between these two strain steps, though for most grains a consistent pattern is found (for grains larger than 4 μm diameter the grains with largest/smallest average strain at $\varepsilon_t = 0.040$ are the same as those with largest/smallest average strain at $\varepsilon_t = 0.126$). As there is significant overlap of the data points for the smaller grains in Fig. 5, the relationship between grain size and $^g\varepsilon_{xx}$ strain for grains with a diameter of less than 5 μm at $\varepsilon_t = 0.126$ is shown in more detail in histogram form in Supplementary Information Fig. S4c.

A similar procedure was carried out for analysis of the change in average orientation of each grain during tensile loading, where for each strain step the average orientation was calculated using renormalization of a simple quaternion sum of all the pixels within the grain, taking care first to condense all orientations to a single cluster in orientation-space [45]. The relationship between grain diameter and rotation angle from the initial to deformed average orientation is shown in Fig. 7 for strains of $\varepsilon_t = 0.040$ and $\varepsilon_t = 0.126$. At each strain level there is a wide spread in the grain-average lattice rotation, with a continuous evolution with strain for most grains. At the final strain of $\varepsilon_t = 0.126$ the average number-weighted rotation angle is close to 4°. The largest change in average orientation is seen for the largest grain examined, but many small size grains also show large rotations in average orientation, though for small size grains most of the data are clustered in the range of ≈ 1°– 4°. Maps showing the change in average grain orientation at these two strain levels are provided in Supplementary Information Figs. S5(a

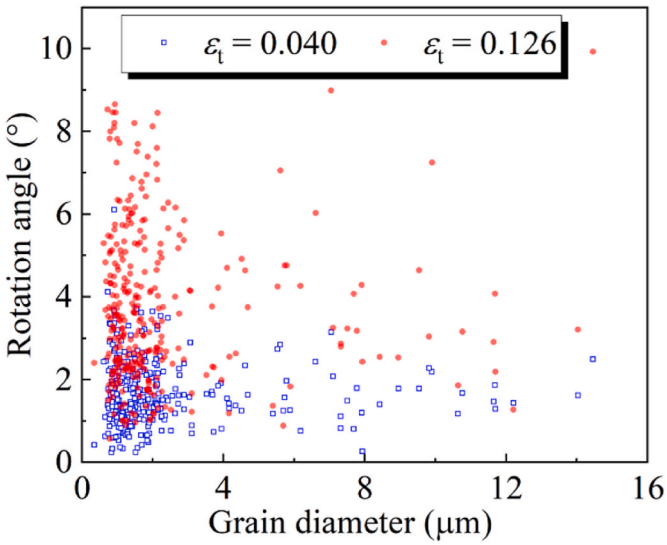

Fig. 7. Rotation of average orientation during deformation to $\varepsilon_t = 0.040$ and $\varepsilon_t = 0.126$for each grain as a function of initial grain diameter.

and b).

The analysis above considers the change in average orientation of each grain. For deformation in tension it is also instructive to examine the change in tensile axis during loading (θ_{TA}), where this is expected to form the majority of the total change in crystallographic orientation (θ_{tot}). These two measures of crystal rotation at the final strain of $\varepsilon_t = 0.126$ are compared in Supplementary Information Fig. S6, where the symbol size indicates the grain size. It is seen that for many grains this is indeed the case, although clearly for some grains, covering a range of sizes, the rotation of the tensile axis is much smaller than the total rotation. These grains are discussed further in section 4.3.

3.5. Strain-normalized grain rotation

An additional measure, that is only possible using combined EBSD-DIC investigations, as in the present experiment, is the average strain-normalized grain rotation (i.e., rotation per unit strain), calculated on the *grain scale* by dividing the change in average grain orientation (relative to the initial orientation of each grain) by the grain-average strain obtained from the DIC measurements ($^{g}\varepsilon_{xx}$). The results of this calculation are shown in Fig. 8a. Note, however that as for the EBSD data grains with initial areas of less than 20 pixels are not considered in this analysis.

The strain-normalized average grain rotation varies over a wide range, from 5° to 158° $^{g}\varepsilon_{xx}{}^{-1}$ (to be read as "grain-average rotation angle in degrees per unit grain-average tensile strain") indicating a high degree of heterogeneity in behavior. Moreover, the highest rotation rates are found for a few of the finest grains. Based on this data, two classes of grain size are defined: (i) near-micrometer grains (NMGs), and (ii) larger grains (LGs), using a dividing threshold of $d_{ECD} = 4$ μm. This value also closely separates the grains expected to arise from the two mixed powders, as seen Fig. 1b (showing cumulative area vs. grain diameter for the SPS material), where 37.5% of the total grain area corresponds grains with diameter less than 4.2 μm.

From the DIC data, the average strain in the NMGs after the final strain step is found to be approx. 40% lower than in the LGs, corresponding to average tensile strain values over these two grain-size classes of 0.098 for the NMGs and 0.135 for the LGs. The average rotation per unit strain of the NMGs is 47° $^{g}\varepsilon_{xx}{}^{-1}$, while the average rotation rate of the LGs is 31° $^{g}\varepsilon_{xx}{}^{-1}$, both of which are close to, but smaller, than the calculated average rotation rate reported in a 3DXRD study of polycrystalline aluminum [46]. The behavior of the NMGs is further analyzed in Fig. 8b, which shows the relationship between grain-averaged strain and rotation angle only for these grains. The inclined line in the figure corresponds to a rotation rate of 70° $^{g}\varepsilon_{xx}{}^{-1}$ (twice the mean value for all grains). The vertical and horizontal dashed-lines in the figure indicate the average strain and rotation angle for the NMGs. It is seen that most of the grains with a rotation rate greater than 70° $^{g}\varepsilon_{xx}{}^{-1}$ have a rotation (change in average orientation) higher than the average value, and almost all of these grains have an individual grain-average strain lower than the average value for all grains.

4. Discussion

4.1. Combined EBSD and DIC measurements

The results show that by controlled use of colloidal silica particles as markers it is possible to repeatedly obtain both EBSD and DIC information during an in-situ experiment. The transparency of the colloidal silica markers to the EBSD signal is reflected by the fact that on undeformed samples decorated by the markers, EBSD maps with indexed fractions of >95% can be achieved (without the use of correction algorithms). The colloidal silica markers do not, however, have as good signal contrast as the "gold-standard" DIC markers, which at present happen also to be gold nanoparticles [47,48]. As a result of the lower contrast, it was found necessary in this study to use a relatively large DIC window size of 59 × 59 pixels in order to obtain correlation results over most of the tracked area. Combined with the fact that the DIC data were calculated from a single SEM images covering the tracked area, this places some limitation on the achievable spatial resolution. For example, slip bands seen in the electron channeling contrast images after deformation to $\varepsilon_t = 0.126$ (Fig. 4d), are not resolved in the DIC maps, whereas with Au nanoparticles, such features can be sharply defined [47,48]. Ongoing work using DIC over a similar area but using a montage of images collected at higher magnification has shown that such slip band features can be resolved, though still not quite as clearly as using Au nanoparticles. The contamination associated with repeated EBSD mapping of the same area still leads to degradation of signal quality, limiting the number of strain steps where both DIC and EBSD are be collected during an in-situ experiment.

4.2. In-grain orientation spread during tension

Inspection of the maps showing misorientation to initial orientation (Fig. 3) reveals some heterogeneity in the crystal lattice rotations within each grain. Here we investigate further this heterogeneity by examining the spread and overall change in tensile axis direction for individual grains during in-situ loading. It is of interest here also to compare the pattern of tensile axis rotation for grains in this sample with those reported previously for aluminium with more conventional grain sizes (i.e. grain diameters of tens of micrometers) based on a 3D X-ray synchrotron

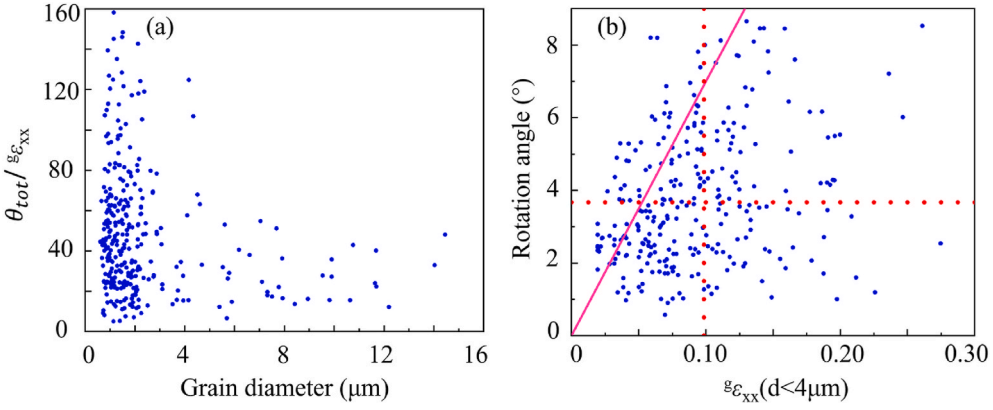

Fig. 8. (a) Variation of strain-normalized grain rotation as a function of grain size; (b) relationship between average rotation angle and average strain for the near-micrometer grains (NMGs). In (b) the diagonal solid magenta line denotes a rotation rate of 70° $^{g}\varepsilon_{xx}{}^{-1}$; red dashed lines show the average rotation angle and average strain for the NMGs. (For interpretation of the references to color in this figure legend, the reader is referred to the Web version of this article.)

study [49].

For this analysis we consider initially the behavior of the larger grains (LGs, as defined as in section 3.5 with diameter > 4 μm). For better statistics, data from the EBSD maps already presented in this paper are supplemented by 35 grains with diameter > 4 μm (to give a total of 73 LGs) from another nearby region in the same tensile sample, where orientations were also measured using EBSD both before and after each strain step, and where a similar pattern of rotations was seen in the EBSD data.

For each of the LGs an inverse pole figure (IPF) was constructed showing the distribution of tensile axis direction at each loading step. Inspection of the IPF maps reveals that the evolution of in-grain tensile axis (TA) spread can be divided into the following four categories, as illustrated in Fig. 9:

Type A: moderate TA spread, characterized by a single rotation path with a similar superimposed spread in the TA distribution;
Type B: a wider and more complex TA spread, often with a split into two parts at the highest strain, where the overall rotation still follows loosely the change in average orientation;
Type C: well-defined TA axis spread not following the change in average TA direction; and
Type D: ill-defined spread in TA at each strain with only a very small rotation-in the average TA direction.

The tensile axis rotations for all 73 LGs are summarized in Fig. 10. Just under half (47%; 34/73) of these grains are Type A, with the other three types accounting for 22%, 16% and 16%, of the grains, respectively. For the Type A grains, where the rotation path of the tensile axis is well-defined, the rotation path of most grains (26 out of 34 grains) follows an orientation dependence in good agreement with previously reported results for aluminium with a significantly larger grain size [49]. The rotation paths for the remaining 8 Type A grains, however, follow a different pattern (indicated by 'blue tails'), which may be due to either the influence of surrounding grains, the fact that only part of each grain is sampled during the present 2D examination, or the smaller grain size compared to previous studies. For the Type B grains, where there is a split in the tensile axis rotation pattern, the average orientation represents less well the grain behaviour, resulting in a less consistent pattern in tensile axis rotation. For type C and D grains the rotation in tensile axis direction is only small, and is therefore also weakly defined.

The tensile axis rotations for the NMGs have also been analyzed. Due, however to the smaller number of EBSD measurements within these grains, the tensile axis spread is less well defined and so here we only analyze the rotation path in the average tensile axis of the NMGs with high rotation angle (>4°). For these grains it was also checked that none showed a split in the tensile axis spread. The results are shown in Fig. 11. In this figure grains where the rotation in tensile axis follows the expected path are marked by red tails, and blue tails are again used to highlight grains that follow a different rotation path to that expected, based on the previously reported data for conventional grain size aluminum [49]. It can be seen that the NMGs show a complex pattern of tensile axis rotation, with many grains showing a large lattice rotation during tension in an unexpected direction, suggesting that the deformation of some small grains may be influenced by factors such as the size, strain, and orientation, of the surrounding grains.

4.3. Deformation in materials with a transmodal grain-size distribution

Although this mixed powder sample can be characterized as bimodal, it is important to also recall that in this material the variation in length scale corresponds to a mixture of two partly overlapping distributions where the individual modal values span a transition in mechanical properties. For this reason, the grain size distribution in the present sample is better described as transmodal, reflecting this combination of characteristics. Additionally, it has been shown elsewhere [50] that changes in dislocation patterning for aluminum take place in the length scale (and strain) regime covered in the present study. In that study of samples deformed 30% in compression it was found that conventional dislocation patterning, including the formation of extended planar boundaries, takes place for grain sizes above ≈7 μm, with a transition to a cell structure for grains with grain size less than ≈3 μm, and only loose dislocation tangles present in grains of less than ≈1 μm diameter. The effect of these changes on texture evolution has not been explored in detail, but it is known that secondary slip system activity is driven by stresses established through dislocation patterning [51] and as such this may contribute to the differences in pattern of tensile axis rotation seen not only for the smallest grains but also in some larger

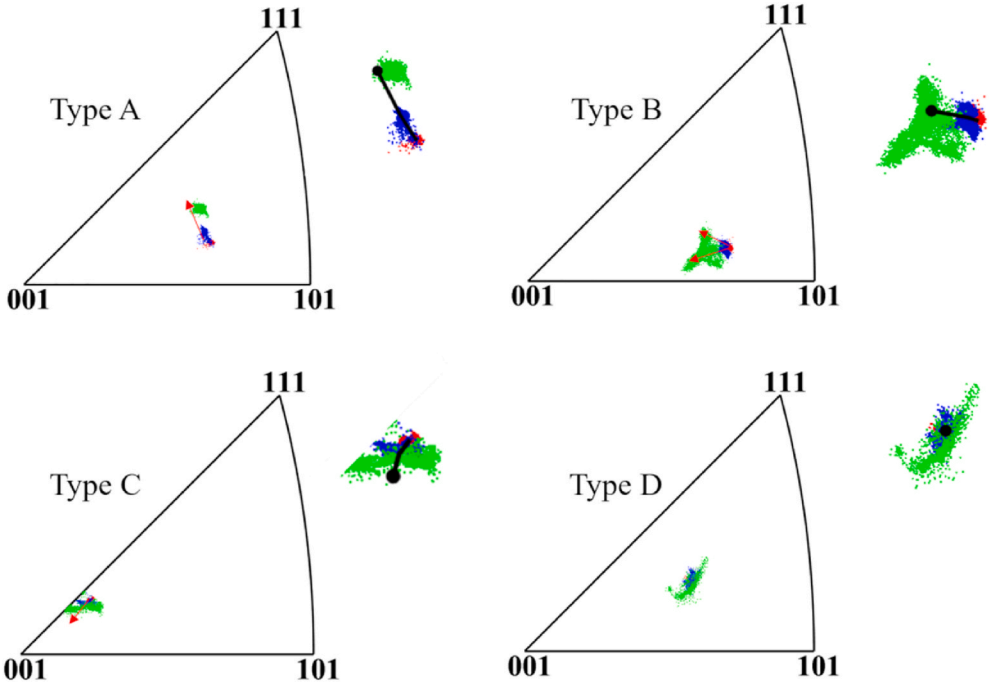

Fig. 9. Characteristic types of spread in tensile axis during loading – the corresponding rotation in tensile axis based on the change in average orientation for each grain is shown in the magnified view on the right-hand side of each inverse triangle. Red, blue and green points represent the undeformed state and tensile strains of $\varepsilon_t = 0.040$ and 0.126, respectively, and red arrows represent rotation trends. In the magnified views a black circle point represents the tensile axis corresponding to the average grain orientation at $\varepsilon_t = 0.126$; the attached black line ends at the tensile axis corresponding to the initial orientation. (For interpretation of the references to color in this figure legend, the reader is referred to the Web version of this article.)

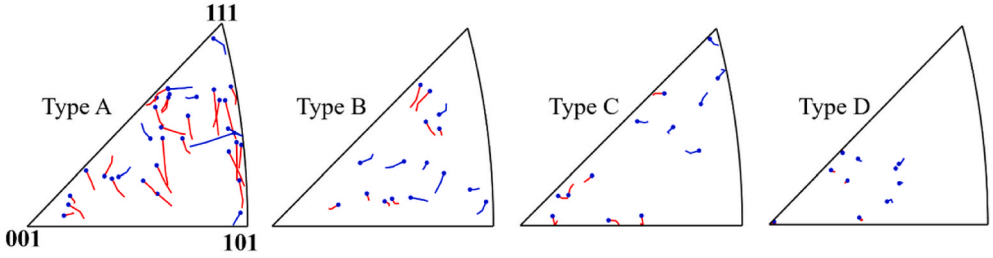

Fig. 10. Rotation of tensile axis during deformation for larger grains (LGs) identified as Type A, B, C and D. Blue points show the tensile axis direction corresponding to the mean orientation of each grain after the final deformation step; the tail is drawn connecting the tensile axis corresponding to the mean orientation at each deformation step (terminated at the initial undeformed state). Rotations that differ significantly from those reported for conventional grain-size samples [49] are shown with blue tails. (For interpretation of the references to color in this figure legend, the reader is referred to the Web version of this article.)

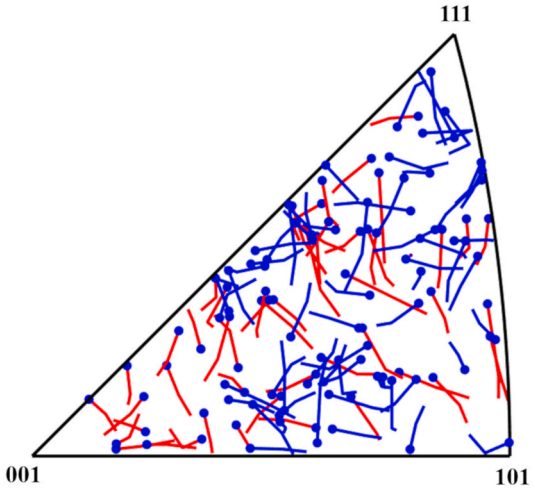

Fig. 11. Rotation of tensile axis during deformation for NMGs with high overall rotation angle (>4°). See Fig. 10 for meaning of the blue and red tails. (For interpretation of the references to color in this figure legend, the reader is referred to the Web version of this article.)

grains.

Despite good mixing of the powders, some clustering of grains from the finer powder is still present, and in fact necessary for space filling requirements. To examine if this also has any influence on the deformation pattern the positions of grains (outlined in white) with either a high rotation angle (>4°), a high rotation rate (>70° ${}^{g}\varepsilon_{xx}{}^{-1}$), an unexpected tensile axis (TA) rotation direction, or a large non-TA rotation component ($\theta_{tot}/\theta_{TA} > 2$), were superposed on the DIC map showing the strain distribution at the end of the experiment (see Supplementary Information Fig. S7(a-c). For each case no strong correlation is seen between the locations of grains with these characteristics, the local strain pattern and regions with obvious clustering of the NMGs. Some preference for NMGs with high rotation angle to be found in small clusters is, however, seen, with somewhat expectedly no clear correlation to the regions of highest macroscopic strain. It could be hypothesized that clusters of NMGs may act as hard volumes, leading to more deformation in neighboring LGs, as may be expected in a hard-soft composite material. No evidence, however, is seen for this, although the spatial distribution of the smallest grains clearly plays some role on the overall strain heterogeneity, as the largest areas with lowest plastic strain are associated with clusters of the small grains. It may be relevant here, however, that in the smallest grains very little dislocation storage is expected [50], and hence these grains will not work-harden and thus become relatively less hard compared to the larger grains during tensile loading. It is also important to note that the NMGs with high rotation per unit strain (or with unusual tensile axis rotations) are in general not located between LGs with high average strain, and show no clear correlation with local strain concentration. It is expected nevertheless that the complex pattern of deformation heterogeneity is linked to the strain compatibility between the differently sized grains, with a larger grain neighbor interaction effect than found in conventional aluminum samples with a unimodal grain size distribution.

Although, based on the results in this study, it is not possible to account directly for the pattern of both local strain and rotation with regard to the grain size heterogeneity, it is possible to note that neither the grain orientation, the grain size, nor the mesoscale grain arrangement (in terms of clustering of the NMGs) can explain the observations. Further insights into the pattern of strain localization on the grain scale may however be possible from the combined use of crystal plasticity finite element modelling, where the ability to provide data both from EBSD and from DIC can be fed into the models for calibration and/or verification.

The present experiment relies on 2D observations, both in terms of the data obtained from the DIC investigation (where only in-plane surface displacements are followed) and also with regard to the fact that grains are tracked on the sample surface. This may have some influence on the results. For the larger grains, however, the orientation dependence of the tensile axis rotations follows that expected from the previous 3D X-ray synchrotron-based investigations, suggesting that the stress-state experienced by these grains (and presumably by extension the NMGs between these grains) should be similar at least to those in bulk material.

4.4. Relationship to overall mechanical properties

In terms of the overall mechanical response, a simple rule of mixtures for the yield stress gives a value of 113 MPa (compared to the measured value of 95 MPa), suggesting that the yielding is weighed towards the larger grain size component. An alternative calculation for the yield stress can be made, based on the Hall-Petch parameters of $\sigma_0 = 20$ MPa and $k_{HP} = 140$ MPaμm$^{0.5}$ [2]. The mean boundary spacing is calculated from the stereological relationship $d = 2/S_V$, where S_V is taken from the volume weighted contributions of the grains from each powder component, i.e., $S_V = 0.375(2/d_{1\mu m}) + 0.625(2/d_{6\mu m})$ with $d_{1\mu m}$ and $d_{6\mu m}$ as the mean grain sizes of the two powders (i.e., 1.2 μm and 4.4 μm, respectively). This gives a value for $S_V = 0.91$ μm^{-1} (and thus $d = 1.1$ μm), leading to a similar estimated yield stress of 114 MPa. It should be recalled here that the value of $k_{HP} = 140$ MPaμm$^{0.5}$ already reflects significantly enhanced strengthening associated with near-micrometer sized grains (cf. $k_{HP} = 40$ MPaμm$^{0.5}$ for conventional grain size aluminium [52]). From the DIC data at the lowest strain studied in the present experiment ($\varepsilon_t = 0.006$) the LGs with a volume fraction of 63% carry 75% of the total strain, showing that while deformation is transferred as expected partly to the larger grains, the NMGs still undergo appreciable plasticity. Additional studies in the ultra low strain regime, using X-ray synchrotron diffraction, are underway to explore the onset of plastic deformation in the near-yield point regime at strains below $\varepsilon_t = 0.006$ [53].

With regard to ductility, as reported above, regions with clusters of NMGs tend to undergo smaller strains, however the extent to which this leads to macroscopic strain localization preceding tensile instability cannot be inferred from the present data set. Further studies on samples with different fractions of mixed powders are in progress and experiments of the kind presented here, where EBSD and DIC are performed for microstructures with different grain size characteristics are expected, to provide answers to this question and as well as to lead to a better understanding, of influence of grain size heterogeneity on mechanical properties.

5. Conclusions

Samples of aluminum prepared using SPS from a mixture of coarse (average powder particle size of 6 μm) and fine (average powder particle size of 1 μm) powders have a microstructure with a transmodal grain size distribution, where in this work, grains with diameters <4 μm (near-micrometer grains, NMGs) are distinguished from grains with larger diameters (larger grains, LGs). The deformation behavior of the sample has been studied during in-situ tensile loading to a strain of $\varepsilon_t = 0.126$ to examine the influence of grain size and spatial distribution on heterogeneity in plastic deformation. Based on the results the following conclusions may be drawn regarding the deformation of this material:

(a) Strain concentrations are found predominantly in the largest grains in the LG subset, with some evidence also for mesoscopic strain localization. Regions of lowest strain are found to correspond predominantly to clusters of NMGs. After the final strain step (corresponding to an average tensile strain for all grains of $\varepsilon_t = 0.126$) the NMGs undertake approx. 40% less strain than the LGs, with average DIC-determined strain values of 0.098 for the NMGs and 0.135 for the LGs.
(b) Unexpectedly, the average rotation rate of the NMGs is slightly higher than that of the LGs, with the NMGs also exhibiting a much wider spread in rotation rate, showing that these grains nevertheless play an important role in the deformation accommodation process in this transmodal grain-sized sample.
(c) Both the LGs and NMGs show a heterogeneous pattern of crystal rotation during tension, both including intragranular rotation and overall rotation. In agreement with previous studies [50] some NMGs are found where no clear evidence of grain sub-division during deformation can be identified.
(d) For the LGs where the average orientation is a good measure of the grain rotation (approx. half of these grains) a clear orientation dependence is found of the tensile axis rotation during deformation, matching that seen in earlier studies of samples with a larger average grain size. A larger fraction of the NMGs show unexpected tensile axis rotations. Neither the grain size, grain orientation, nor the grain arrangement can completely explain the observations relating to the spatial distribution of local crystal rotations and plastic strain.

The experiments also provide a clear demonstration that use of colloidal silica as surface markers allows the repeatedly collection of both DIC and EBSD data in the same area during tensile loading, thereby enabling a correlation between both lattice rotations and strain distribution as a function of grain size. In this regard the ability to perform both DIC and EBSD measurements on the same sample during in-situ deformation provides the opportunity to obtain rich data sets for investigation of plastic deformation, in particular in the case of samples with a heterogeneous microstructure.

CRediT authorship contribution statement

W.Q. Gao: Investigation, Writing – original draft, Formal analysis, Data curation. **C.L. Zhang:** Investigation, Software. **M.X. Yang:** Investigation, Resources. **S.Q. Zhang:** Investigation, Resources. **D. Juul Jensen:** Conceptualization, Writing – review & editing. **A. Godfrey:** Supervision, Funding acquisition, Writing – review & editing.

Declaration of competing interest

The authors declare that they have no known competing financial interests or personal relationships that could have appeared to influence the work reported in this paper.

Acknowledgments

AG and GWQ gratefully acknowledge financial support from the National Key Research and Development Program of China (2016YFB0700403) and the National Natural Science Foundation of China (grant number 51671113). MY is funded by the National Natural Science Foundation of China (grant number 52071326). DJJ acknowledges the support from the European Research Council (ERC) under the European Union's Horizon 2020 research and innovation programme (grant agreement No. 788567, M4D).

Appendix A. Supplementary data

Supplementary data to this article can be found online at https://doi.org/10.1016/j.msea.2021.142010.

Data availability

The raw/processed data required to reproduce these findings cannot be shared at this time as the data also forms part of an ongoing study.

References

[1] X. Huang, N. Hansen, N. Tsuji, Hardening by annealing and softening by deformation in nanostructured metals, Science 312 (2006) 249–251.
[2] G.M. Le, A. Godfrey, N. Hansen, Structure and strength of aluminum with sub-micrometer/micrometer grain size prepared by spark plasma sintering, Mater. Des. 49 (2013) 360–367.
[3] K.N. Zhu, A. Godfrey, N. Hansen, X.D. Zhang, Microstructure and mechanical strength of near- and sub-micrometre grain size copper prepared by spark plasma sintering, Mater. Des. 117 (2017) 95–103.
[4] N. Tsuji, Y. Ito, Y. Saito, Y. Minamino, Strength and ductility of ultrafine grained aluminum and iron produced by ARB and annealing, Scripta Mater. 47 (2002) 893–899.
[5] Y.Z. Tian, S. Gao, L.J. Zhao, S. Lu, R. Pippan, Z.F. Zhang, N. Tsuji, Remarkable transitions of yield behavior and Luders deformation in pure Cu by changing grain sizes, Scripta Mater. 142 (2018) 88–91.
[6] X.L. Wu, F.P. Yuan, M.X. Yang, P. Jiang, C.X. Zhang, L. Chen, Y.G. Wei, E. Ma, Nanodomained nickel unite nanocrystal strength with coarse-grain ductility, Sci. Rep. 5 (2015) 1–10.
[7] K. Lu, Making strong nanomaterials ductile with gradients, Science 345 (2014) 1455–1456.
[8] Y. Zhu, K. Ameyama, P.M. Anderson, I.J. Beyerlein, H. Gao, H.S. Kim, E. Lavernia, S. Mathaudhu, H. Mughrabi, R.O. Ritchie, N. Tsuji, X. Zhang, X. Wu, Heterostructured materials: superior properties from hetero-zone interaction, Mater. Res. Lett. 9 (2020) 1–31.
[9] T.H. Fang, W.L. Li, N.R. Tao, K. Lu, Revealing extraordinary intrinsic tensile plasticity in gradient nano-grained copper, Science 331 (2011) 1587–1590.
[10] Z. Cheng, H.F. Zhou, Q.H. Lu, H.J. Gao, L. Lu, Extra strengthening and work hardening in gradient nanotwinned metals, Science 362 (2018), eaau1925.
[11] J. Li, M. Zhao, L. Jin, F. Wang, S. Dong, J. Dong, Simultaneously improving strength and ductility through laminate structure design in Mg–8.0Gd–3.0Y-0.5Zr alloys, J. Mater. Sci. Technol. 71 (2021) 195–200.
[12] Z. Zhang, S.K. Vajpai, D. Orlov, K. Ameyama, Improvement of mechanical properties in SUS304L steel through the control of bimodal microstructure characteristics, Mater. Sci. Eng. A 598 (2014) 106–113.
[13] P.V. Liddicoat, X.Z. Liao, Y.H. Zhao, Y.T. Zhu, M.Y. Murashkin, E.J. Lavernia, R. Z. Valiev, S.P. Ringer, Nanostructural hierarchy increases the strength of aluminium alloys, Nat. Commun. 1 (2010) 1–7.
[14] S.K. Vajpai, M. Ota, T. Watanabe, R. Maeda, T. Sekiguchi, T. Kusaka, K. Ameyama, The development of high performance Ti-6Al-4V alloy via a unique microstructural design with bimodal grain size distribution, Metall. Mater. Trans. 46 (2015) 903–914.
[15] M. Calcagnotto, Y. Adachi, D. Ponge, D. Raabe, Deformation and fracture mechanisms in fine- and ultrafine-grained ferrite/martensite dual-phase steels and the effect of aging, Acta Mater. 59 (2011) 658–670.

[16] M.J.N.V. Prasad, S. Suwas, A.H. Chokshi, Microstructural evolution and mechanical characteristics in nanocrystalline nickel with a bimodal grain-size distribution, Mater. Sci. Eng. A 503 (2009) 86–91.
[17] T. Morimitsu, N. Takata, D. Terada, N. Tsuji, Analysis of deformation behaviors of ultrafine grained Cu-30%Zn with bimodal grain-size distribution, J. Phys. Conf. Ser. 240 (2010), 012015.
[18] G.J. Fan, H. Choo, P.K. Liaw, E.J. Lavernia, Plastic deformation and fracture of ultrafine-grained Al-Mg alloys with a bimodal grain size distribution, Acta Mater. 54 (2006) 1759–1766.
[19] S.H. Xia, L.V. Vychigzhanina, J.T. Wang, I.V. Alexandrov, Enhanced strength and ductility in hypo-eutectoid Cu-Al alloys through ECAP and annealing, Mater. Sci. Forum 584 (2008) 315–326.
[20] D. Orlov, Y. Todaka, M. Umemoto, N. Tsuji, Formation of bimodal grain structures in high purity Al by reversal high pressure torsion, Scripta Mater. 64 (2011) 498–501.
[21] H. Jin, D.J. Lloyd, Effect of a duplex grain size on the tensile ductility of an ultra-fine grained Al–Mg alloy, AA5754, produced by asymmetric rolling and annealing, Scripta Mater. 50 (2004) 1319–1323.
[22] D. Witkin, Z. Lee, R. Rodriguez, S. Nutt, E. Lavernia, Al-Mg alloy engineered with bimodal grain size for high strength and increased ductility, Scripta Mater. 49 (2003) 297–302.
[23] M.S. Oskooie, H. Asgharzadeh, Strength and ductility enhancement in nanostructured AI6063 with a bimodal grain size distribution, IOP Conf. Ser. Mater. Sci. Eng. 63 (2014), 012022.
[24] D.P. Zhao, Y. Liu, F. Liu, Y.R. Wen, L.J. Zhang, Y.H. Dou, ODS ferritic steel engineered with bimodal grain size for high strength and ductility, Mater. Lett. 65 (2011) 1672–1674.
[25] B. Flipon, C. Keller, L.G. de la Cruz, E. Hug, F. Barbe, Tensile properties of spark plasma sintered AISI 316L stainless steel with unimodal and bimodal grain size distributions, Mater. Sci. Eng. A 729 (2018) 249–256.
[26] C. Zhu, T. Harrington, G.T. Gray, K.S. Vecchio, Dislocation-type evolution in quasi-statically compressed polycrystalline nickel, Acta Mater. 155 (2018) 104–116.
[27] B. Pan, K.M. Qian, H.M. Xie, A. Asundi, Two-dimensional digital image correlation for in-plane displacement and strain measurement: a review, Meas. Sci. Technol. 20 (2009), 062001.
[28] S.-W. Khoo, S. Karuppanan, C.-S. Tan, A review of surface deformation and strain measurement using two-dimensional digital image correlation, Metrol. Meas. Syst. 23 (2016) 461–480.
[29] A. Godfrey, O.V. Mishin, Q. Liu, Processing and interpretation of EBSD data gathered from plastically deformed metals, Mater. Sci. Technol. 22 (2006) 1263–1270.
[30] A. Harte, M. Atkinson, M. Preuss, J.Q. da Fonseca, A statistical study of the relationship between plastic strain and lattice misorientation on the surface of a deformed Ni-based superalloy, Acta Mater. 195 (2020) 555–570.
[31] A.D. Kammers, S. Daly, Small-scale patterning methods for digital image correlation under scanning electron microscopy, Meas. Sci. Technol. 22 (2011) 125501.
[32] N. Sabate, D. Vogel, J. Keller, A. Gollhardt, J. Marcos, I. Gracia, C. Cane, B. Michel, FIB-based technique for stress characterization on thin films for reliability purposes, Microelectron. Eng. 84 (2007) 1783–1787.
[33] A. Tatschl, O. Kolednik, A new tool for the experimental characterization of micro-plasticity, Mater. Sci. Eng. A 339 (2003) 265–280.
[34] N. Biery, M. De Graef, T.M. Pollock, A method for measuring microstructural-scale strains using a scanning electron microscope: applications to gamma-titanium aluminides, Metall. Mater. Trans. 34 (2003) 2301–2313.
[35] M.A. Tschopp, B.B. Bartha, W.J. Porter, P.T. Murray, S.B. Fairchild, Microstructure-dependent local strain behavior in polycrystals through in-situ scanning electron microscope tensile experiments, Metall. Mater. Trans. 40 (2009) 2363–2368.
[36] C.B. Montgomery, B. Koohbor, N.R. Sottos, A robust patterning technique for electron microscopy-based digital image correlation at sub-micron resolutions, Exp. Mech. 59 (2019) 1063–1073.
[37] T.T. Zhang, J. Jiang, B.A. Shollock, T.B. Britton, F.P.E. Dunne, Slip localization and fatigue crack nucleation near a non-metallic inclusion in polycrystalline nickel-based superalloy, Mater. Sci. Eng. A 641 (2015) 328–339.
[38] E. Polatidis, W.N. Hsu, M. Smid, H. Van Swygenhoven, A high resolution digital image correlation study under multiaxial loading, Exp. Mech. 59 (2019) 309–317.
[39] S.Q. Zhang, A. Godfrey, C.L. Zhang, W. Liu, D. Juul Jensen, Surface patterning for combined digital image correlation and electron backscatter diffraction in-situ deformation experiments, Mater. Char. 164 (2020) 110332.
[40] W.Q. Gao, C.L. Zhang, S.Q. Zhang, A. Godfrey, In-situ study of microstructural evolution and local strain distribution during tensile loading of near-micrometre grain size aluminium, IOP Conf. Ser. Mater. Sci. Eng. 580 (2019), 012031.
[41] C.Y.J. Barlow, B. Bay, N. Hansen, A comparative investigation of surface relief structures and dislocation microstructures in cold-rolled aluminium, Philos. Mag. A 51 (1985) 253–275.
[42] V. Randle, N. Hansen, D. Juul Jensen, The deformation behaviour of grain boundary regions in polycrystalline aluminium, Philos. Mag. A 73 (2006) 265–282.
[43] X. Hong, A. Godfrey, C.L. Zhang, W. Liu, A. Chapuis, Investigation of grain subdivision at very low plastic strains in a magnesium alloy, Mater. Sci. Eng. A 693 (2017) 14–21.
[44] P.S. Bate, R.D. Knutsen, I. Brough, F.J. Humphreys, The characterization of low-angle boundaries by EBSD, J. Microsc. 220 (2005) 36–46.
[45] W. Pantleon, Retrieving orientation correlations in deformation structures from orientation maps, Mater. Sci. Technol. 21 (2005) 1392–1396.
[46] L. Margulies, G. Winther, H.F. Poulsen, In situ measurement of grain rotation during deformation of polycrystals, Science 291 (2001) 2392–2394.
[47] A.D. Kammers, S. Daly, Self-assembled nanoparticle surface patterning for improved digital image correlation in a scanning electron microscope, Exp. Mech. 53 (2013) 1333–1341.
[48] R. Sperry, A. Harte, J.Q. da Fonseca, E.R. Homer, R.H. Wagoner, D.T. Fullwood, Slip band characteristics in the presence of grain boundaries in nickel-based superalloy, Acta Mater. 193 (2020) 229–238.
[49] H.F. Poulsen, L. Margulies, S. Schmidt, G. Winther, Lattice rotations of individual bulk grains - Part I: 3D X-ray characterization, Acta Mater. 51 (2003) 3821–3830.
[50] G.M. Le, A. Godfrey, N. Hansen, W. Liu, G. Winther, X. Huang, Influence of grain size in the near-micrometre regime on the deformation microstructure in aluminium, Acta Mater. 61 (2013) 7072–7086.
[51] D. Kuhlmann Wilsdorf, N.R. Comins, Dislocation cell-formation and work-hardening in the unidirectional glide of Fcc metals .1. Basic theoretical-analysis of cell-walls parallel to the primary glide plane in early stage-I, Mater. Sci. Eng. 60 (1983) 7–24.
[52] N. Hansen, The effect of grain size and strain on the tensile flow stress of aluminium at room temperature, Acta Mater. 25 (1977) 863–869.
[53] C.L. Zhang, A. Godfrey, Y. Zhang, G.L. Wu, R. Xu, W. Liu, D. Juul Jensen, Dislocation density in fine grain-size spark-plasma sintered aluminum measured using high brightness synchrotron radiation, Mater. Lett. 269 (2020) 127653.